Journal of Nanobiotechnology

RESEARCH

Open Access

A collagenase-decorated Cu-based nanotheranostics: remodeling extracellular matrix for optimizing cuproptosis and MRI in pancreatic ductal adenocarcinoma

Yining Wang[1†], Qiaomei Zhou[1†], Wangping Luo[1], Xiaoyan Yang[1], Jinguo Zhang[1], Yijie Lou[3], Jin Mao[1], Jiayi Chen[2], Fan Wu[4], Jue Hou[2], Guping Tang[2], Hongzhen Bai[2*] and Risheng Yu[1*]

Abstract

Pancreatic ductal adenocarcinoma (PDAC), characterized by a dense extracellular matrix (ECM), presents significant therapeutic challenges due to its poor prognosis and high resistance to chemotherapy. Current chemodrugs and diagnostic agents largely fail to cross the barrier posed by the ECM, which severely limits the PDAC theranostics. This study introduces a novel theranostic strategy using thioether-hybridized hollow mesoporous organosilica nanoparticles (dsMNs) for the co-delivery of copper (Cu) and disulfiram (DSF), aiming to induce cuproptosis in PDAC cells. Our approach leverages the ECM-degrading enzyme collagenase, integrated with dsMNs, to enhance drug penetration by reducing matrix stiffness. Furthermore, the innovative use of a pancreatic cancer cell membrane coating on the nanoparticles enhances tumor targeting and stability (dsMCu-D@M-Co). The multifunctional platform not only facilitates deep drug penetration and triggers cuproptosis effectively but also utilizes the inherent properties of Cu to serve as a T1-weighted magnetic resonance imaging (MRI) contrast agent. In vitro and in vivo assessments demonstrate significant tumor size reduction in PDAC-bearing mice, highlighting the dual functionality of our platform in improving therapeutic efficacy and diagnostic precision. This integrated strategy represents a significant advancement in the management of PDAC, offering a promising new direction for overcoming one of the most lethal cancers.

[†]Yining Wang and Qiaomei Zhou contributed equally to this work.

*Correspondence:
Hongzhen Bai
hongzhen_bai@zju.edu.cn
Risheng Yu
risheng-yu@zju.edu.cn

Full list of author information is available at the end of the article

Graphical Abstract

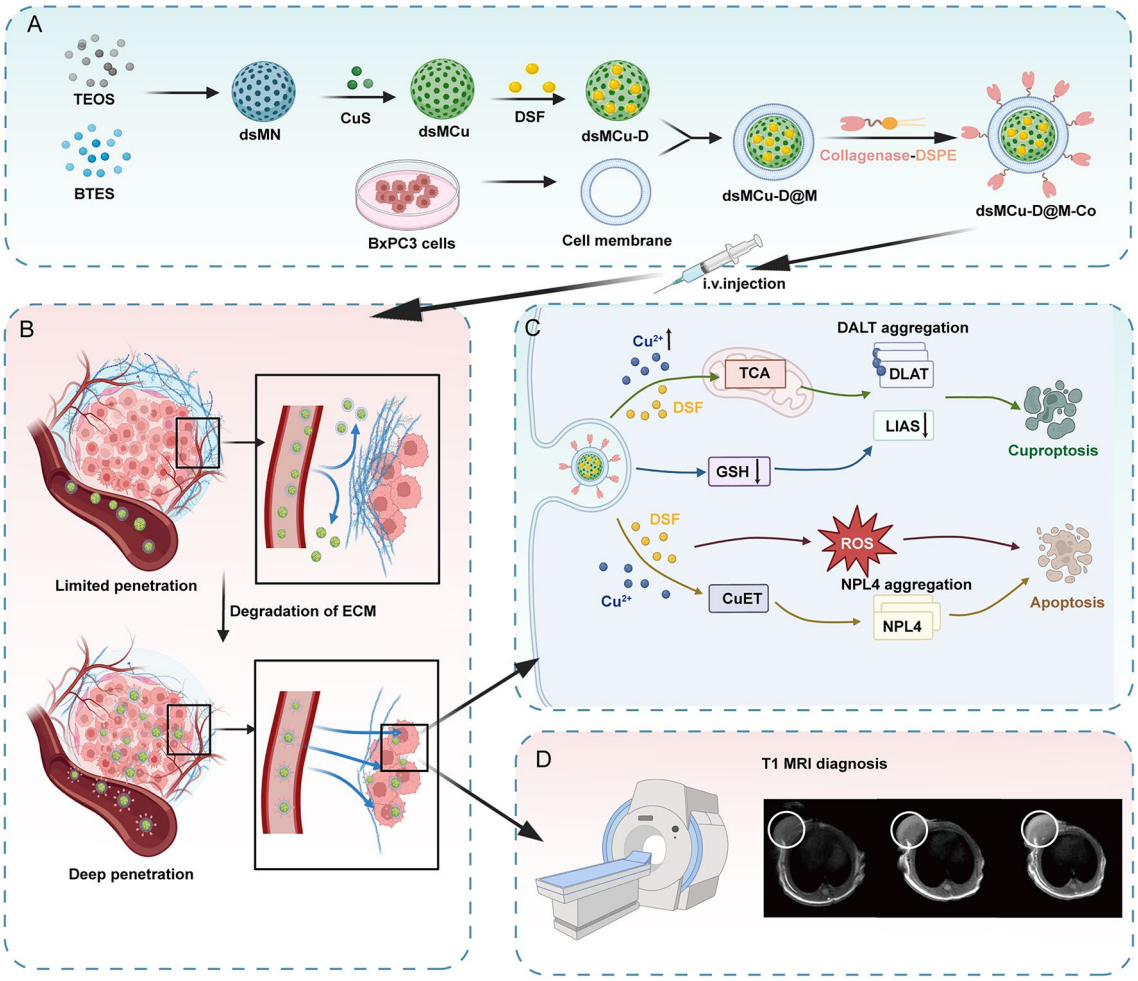

Keywords Pancreatic ductal adenocarcinoma, Extracellular matrix, Collagenase, Cuproptosis, Magnetic resonance imaging

Background

Pancreatic ductal adenocarcinoma (PDAC) has poor prognosis with a five-year survival rate below 9%, making it the seventh leading cause of cancer-related deaths globally [1, 2]. Early diagnosis and treatment of PDAC poses significant challenges; 80–85% of patients lose the opportunity for surgical intervention by the time of detection [3], leading to the majority of PDAC patients relying on chemotherapy [4]. Numerous anticancer medications, such as frontline PDAC drugs gemcitabine and paclitaxel, have demonstrated to be efficient against PDAC cells in vitro; yet, they have limited efficacy in vivo [5]. Studies have disclosed that the vital factor contributing to the therapeutic challenges in PDAC is the dense extracellular matrix (ECM) surrounding the pancreatic tumor [6–8]. The ECM impedes the effective delivery of chemotherapeutic agents, primarily by orchestrating a notable elevation in interstitial fluid pressure within the tumor microenvironment (TME) [9, 10]. The interstitial fluid pressure of PDAC tumors is nearly ten-fold higher than that of the normal pancreas, significantly compromising tumor permeability [11]. Based on this, we propose that the integration of ECM remodeling with precise drug delivery could have major implications on the treatment of PDAC.

Some of the current delivery systems targeting the ECM primarily address the generation process of the ECM [7, 12, 13]. These strategies can reduce ECM generation and moderately enhance drug penetration, yet, the established ECM still impose limitations on drug penetration [14]. Herein, we posit that the direct disruption of PDAC ECM represents a straightforward way of

achieving deep drug delivery. Collagen, which constitutes up to 90% of the PDAC ECM, plays a critical role determining ECM stiffness and PDAC therapeutic challenge [15]. Clinical trials show that, treated with gemcitabine, patients with high ECM collagen levels have a median overall survival of 6.4 months, whereas patients with low ECM collagen levels have a higher median overall survival of 14.6 months [16]. Collagenases can efficiently degrade collagen, which could attenuate the stiffness of the matrix and contribute to more efficient drug delivery into solid tumors. Evidences have shown an 87% reduction in the tumor size of PDAC-bearing mice treated with a liposomal formulation of collagenase followed by paclitaxel, compared to mice treated with paclitaxel monotherapy [17]. Taken together, these evidences support collagenase anti-collagen strategy can overcome ECM barrier and improve tumor penetration. Therefore, we propose that developing an "all-in-one" collagenase-decorated platform integrating ECM barrier degradation with antitumor mechanism initiation is a promising approach to overcome PDAC drug delivery challenge.

Copper (Cu), an essential transition metal, plays a double-edged sword role in cellular processes. On one hand, it functions as a co-factor for various enzymes by donating or accepting electrons. On the other hand, excessive Cu accumulation can cause a range of cellular metabolic dysfunctions, ultimately leading to cell death [18, 19]. Notably, a Cu-dependent death pathway termed "cuproptosis" has been discovered, which involves intracellular Cu accumulation triggering mitochondrial lipoylated protein (DLAT) aggregation and destabilization of iron–sulfur (Fe–S) cluster proteins such as lipoyl synthase (LIAS) within the tricarboxylic acid (TCA) cycle [20]. Also, its dysregulation has been observed in the microenvironment of malignancies such as PDAC [21, 22]. Therefore, we hypothesize that delivering Cu into PDAC would be a potential therapeutic approach. However, achieving primary cuproptosis is hindered by an insufficient amount of Cu in the TME and the efflux of excess Cu from cells [23]. This renders the precise and efficient delivery of Cu to PDAC cells a critical concern for cuproptosis-based therapy. Disulfiram (DSF), a potential anticancer agent, not only induces ROS-dependent oxidative stress but also facilitates Cu uptake by cells [24]. In PDAC, DSF significantly enhances Cu uptake by tumor cells in relation to free Cu, thereby improving the efficacy of cuproptosis [25, 26]. Furthermore, DSF can combine with Cu ions to form tumor cytotoxic bis(diethyldithiocarbamate)-Cu (CuET), which could promote nuclear protein localization protein 4 (NPL4) aggregation and induce apoptosis [27]. Moreover, owing to its unpaired electrons, Cu has potential as a T_1-weighted magnetic resonance imaging (MRI) contrast agent, which can assist in diagnosing PDAC [28–30]. Hence, the co-delivery of DSF and Cu to tumor tissues using delivery systems is a promising theranostic strategy in PDAC treatment.

In this study, thioether-hybridized hollow mesoporous organosilica nanoparticles (dsMNs) were investigated to co-deliver Cu and DSF. The dsMNs bound to CuS (dsMN-CuS, denoted as dsMCu) via metal coordination and could physically adsorb DSF (dsMCu-D) owing to its hollow mesoporous structure. This biocompatible material had disulfide bonds and responded to high glutathione (GSH) expression in the TME, enabling a precisely controlled release and co-delivery. Moreover, an innovative linker between collagenase and the dsMCu-D platform was developed. PDAC cell membrane-coated NPs with a core–shell structure (dsMCu-D@M) provided stability and enhanced the tumor-targeting functionality in vivo. Furthermore, the phospholipid bilayer of the cell membrane enabled facile modification. Collagenase was decorated into dsMCu-D@M NPs using the "phospholipid insertion method" (dsMCu-D@M-Co) (Scheme 1A). Through homologous targeting, dsMCu-D@M-Co NPs could effectively target PDAC. dsMCu-D@M-Co promoted collagen digestion when NPs reached the tumor site, enhancing the penetration into the PDAC tumor (Scheme 1B). After the uptake of Cu-based NPs, Cu directly engaged with DLAT, fostering the disulfide-bond-dependent aggregation of lipoylated DLAT. LIAS emerged as a pivotal mediator of lipoylation, contributing to the accumulation of noxious lipoylated DLAT and subsequent cuproptosis. Moreover, the formation of CuET induced NPL4 protein aggregation, disrupting these specific processes and culminating in apoptosis (Scheme 1C). Thus, we constructed a multifunctional nanoplatform based on organic–inorganic hybrid materials. In vitro and in vivo experiments demonstrated that our multifunctional nanoplatform not only promoted deep drug penetration but also effectively triggered cuproptosis, significantly reducing tumor size in PDAC-bearing mice. Furthermore, the inherent properties of Cu enhanced T1-weighted MRI, providing a powerful diagnostic tool alongside therapeutic action (Scheme 1D).

Methods

Materials

Cetyltrimethylammonium chloride (CTAC), bis[3-(triethoxysilyl) propyl] tetrasulphide (BTES), triethanolamine (TEA), tetraethyl orthosilicate (TEOS), ethanol, ammonia aqueous solution ($NH_3{\cdot}H_2O$, 25 wt%), and collagenase were sourced from Sigma-Aldrich (MO, USA). (3-mercaptopropyl) trimethoxysilane (MPTES), sodium sulfide nonahydrate ($Na_2S{\cdot}9H_2O$), 3-(4,5-Dimethylthiazol-2-yl)-2,5-diphenyltetrazolium bromide (MTT), sodium citrate, L-glutathione (GSH), 2-iminothiolane (Traut's reagent), copper chloride dihydrate ($CuCl_2{\cdot}2H_2O$), and disulfiram (DSF) were obtained from

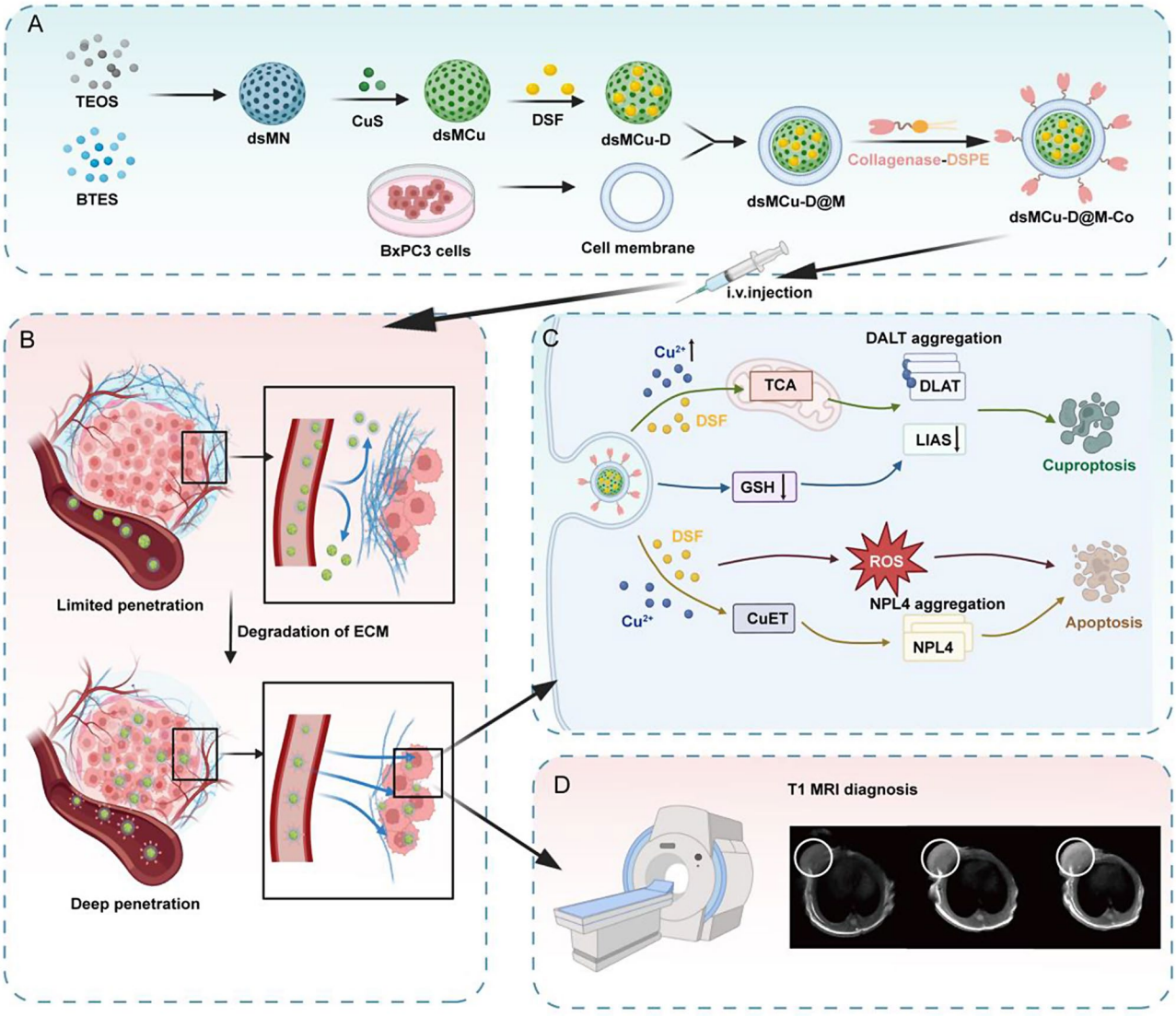

Scheme 1 Synthesis process of dsMCu-D@M-Co NPs for tumor therapy and MRI diagnosis. (**A**) Preparation of dsMCu-D@M-Co. (**B**) dsMCu-D@M-Co accumulated in the tumor tissues after intravenous (i.v.) injection and collagenase effectively degraded the ECM, which enhanced the deep penetration of NPs. (**C**) Schematic illustration of the anticancer effects of dsMCu-D@M-Co on cuproptosis and apoptosis. (**D**) T1 MRI diagnosis

Aladdin Co., Ltd. (Shanghai, China). Additionally, the Membrane and Cytosol Protein Extraction Kit, blotting grade, primary antibody dilution buffer, DCFH-DA, fluorescein isothiocyanate (FITC) and 4'6-diamidino-2-phenylindole (DAPI) were acquired from Beyotime (China).

Cell lines and animals

The BxPC-3 cell line, which originates from human pancreatic cancer, was procured from Procell (Wuhan, China). These cells were maintained in an RPMI 1640 medium containing 10% FBS at 37 °C within a humidified incubator with 5% CO2. Male BALB/c nude mice, aged 6–8 weeks, were sourced from the Shanghai Silaike Laboratory Animal Limited Liability Company. All animal experiments were conducted in accordance with the guidelines set by the National Institutes of Health (NIH, USA) and were approved by the Animal Experiment Committee of Zhejiang University (Approval Year: 2024, No. 040). To generate the BxPC3 tumor-bearing mouse model, 2.0×10^6 cells were subcutaneously injected into the left thigh of male BALB/c nude mice. The volume of the tumor (V) was determined using the formula $V=a^2\times b/2$, where 'a' represents the shortest length (mm) and 'b' represents the longest length (mm) of the tumor.

Synthesis of dsMNs

Initially, TEA (6 g, 10 wt%) and CTAC (40 g, 10 wt%) aqueous solutions were mixed and stirred at 85 °C for 15 min. TEOS (2 ml) was then added dropwise and allowed to react for 1 h. Following this, a mixture of

TEOS (1 ml) and BTES (2 ml) was added, and the reaction was continued for an additional 4 h. The resulting products were washed thrice with ethanol. Then the resulting products were dispersed in 50 mL methanol containing 1 wt% NaCl and heated at 65 °C, to remove the template CTAC. This step was repeated at least three times, each time at least 12 h to ensure the template was removed completely. The final dsMN products were obtained using an ammonia-assisted selective etching strategy, which involved reaction of the NPs with an aqueous solution of ammonia (25 wt%) for 2.5 h at 90 °C. After the solution cooled to room temperature, the final dsMN products were acquired by centrifuging and subsequently washing three times with water [31].

Synthesis of dsMCu

dsMCu were synthesized according to the classical synthesis method. First, 4 mL of a 0.05 M $Na_2S{\cdot}9H_2O$ aqueous solution was added to 200 mL of a mixed solution containing 1 mmol $CuCl_2{\cdot}2H_2O$ and 0.68 mmol sodium citrate. The mixture was stirred at ambient conditions for 30 min, followed by heating to 90 °C and maintaining this temperature for 10 min. This process yielded a dark-green copper sulfide (CuS) NP solution which should be transferred to an ice bath immediately. Next, dsMNs (15 mg) were dispersed in 40 mL ethanol, and a mixture of 0.15 mL MPTES and 0.2 mL $NH_3{\cdot}H_2O$ (25 wt%) was added to it. After stirring overnight, the resulting dsMN-SH was collected via centrifugation and washed thrice with ethanol. Next, 60 mL of the CuS solution and 30 mg dsMN-SH were re-dispersed in 100 mL water and stirred for 2 h in ice bath. The dsMCu NPs were obtained via centrifugation and then washed three times with water [32].

Loading DSF into dsMCu (dsMCu-D)

For incorporating DSF molecules into dsMCu NPs, 10 milligrams of dsMCu NPs were dispersed in 2 milliliter of ethanol solution containing 20 milligrams of DSF, followed by overnight vigorous stirring. Subsequently, the dsMCu-D NPs composite was obtained through centrifugation and washed thrice with ethanol for subsequent applications. Then, the encapsulated dsMCu-D NPs samples are placed into the thermogravimetric analyzer and heated within a specific temperature range. At different temperatures, both the drug and the carrier undergo mass changes. The encapsulation efficiency and drug loading values were calculated by observing the variations in the sample mass.

Extraction and preparation of BxPC-3 cell membrane-coated nanoparticles

BxPC-3 cell membranes were isolated using a membrane protein extraction kit from Beyotime (China), following the manufacturer's guidelines. Initially, BxPC-3 cells were cultured and suspended in reagent A for membrane protein extraction, followed by incubation on ice for 20 min. The cells were then lysed by repeated freezing in liquid nitrogen and subsequent thawing at room temperature until complete lysis was achieved. After centrifugation at 800 g and 4 °C for 15 min to remove intact cells and nuclei, the lysate was further centrifuged at 15,000 g and 4 °C for 40 min to separate out the cell membranes. The supernatant was discarded, and the pellet containing the BxPC-3 cell membranes was collected. To prepare dsMCu-D@M nanoparticles, dsMCu-D was combined with BxPC-3 cell membranes using sonication and then extruded through a 200 nm polyethylene terephthalate membrane (LiposoFast, Avestin, Canada). The resulting dsMCu-D@M nanoparticles were harvested by centrifugation and washed with water [33].

Synthesis of dsMCu-D@M-Co

For the synthesis of dsMCu-D@M-Co, collagenase-modified DSPE-Col was synthesized first. Traut's reagent in a 10 mg/mL concentration and collagenase in a concentration of 10 mg/mL were combined and stirred at room temperature for one hour to synthesize thiolated collagenase (SH-Col). The excess Traut's reagent was removed by dialysis. Then, DSPE-PEG-MAL at 15 mg/mL was mixed with SH-Col at a concentration of 7.5 mg/mL to synthesize DSPE- PEG-Col. The dialysis removed any unbound DSPE- PEG-MAL. The addition of this DSPE-PEG-Col into the dsMCu-D@M and incubation with it at room temperature for one hour allowed the lipids to fuse with the cell membrane [34]. The unconjugated DSPE-Col was dialyzed out. Finally, dsMCu-D@M-Co was centrifuged to obtain the product, which was washed with water.

Collagenase activity study

The residual activity of collagenase was determined first on gelatin. A gelatin solution (30 mg/mL) was incubated at 37 °C with DSPE-Col, free collagenase, dsMCu-D@M, and dsMCu-D@M-Co. After 24 h of incubation, each sample was cooled at four °C for 30 min before being documented with a digital camera. At the same time, activity was assessed by determining collagenase activity using the Collagenase Activity Colorimetric Assay Kit (Sigma-Aldrich, St. Louis, MO, USA). Collagen was mixed with PBS that included FITC (10 μg/mL) and put in ice. Next, the mixture was added to a 24-well plate and allowed to solidify at room temperature for 20 min. When gel appeared, it was softly washed till the fluorescence of the supernatant became zero [35]. After that, 200 μL of PBS, dsMCu-D@M, dsMCu-D@M-Co, and collagenase were applied on the surface of the gel. After

24 h of incubation at 37 °C, the fluorescence in the supernatant was measured.

Characterization

The particle size and zeta potential were determined using a Litesizer500 particle analyzer (Anton-Paar, Austria). The structural features of the dsMN, dsMCu, dsMCu-D@M, and dsMCu-D@M-Co nanoparticles were investigated using the transmission electron microscopy (TEM) JEM-1400fash JEOL, Japan. The surface area and pore size distribution were determined by the Brunauer-Emmett-Teller (BET) and Barrett-Joyner-Halenda (BJH) techniques. Ultraviolet absorption spectra were determined on a UV-2600 spectrophotometer by SHIMADZU, Japan. Fourier transform infrared (FTIR) spectra were recorded using a 330FT-IR spectrometer produced by Thermo Fisher Scientific, USA. The copper content of the samples was determined by inductively coupled plasma mass spectrometry with a Nexion 300X instrument from PerkinElmer, USA. The loading percentage of the drug was determined using a thermogravimetric analyzer, and the drug loading was calculated by dividing the weight of DSF by the total weight of the drug-loaded product and multiplying the whole by 100%.

Collagen degradation in vitro

BxPC-3 cells were seeded in an 8-chamber slide overnight for adhesion. The cells were washed with PBS, and a fresh medium containing different NPs was added. After two PBS rinses, the cells were fixed with 4% formaldehyde for 10 min. Collagen was immunostained using an Anti-Collagen I antibody according to the manufacturer's instructions, and imaging was performed using confocal laser scanning microscopy (CLSM).

Assessing cellular uptake

BxPC-3 cells were plated onto 8-chamber slides (Cellvis, USA) and incubated overnight at 37 °C with 5% CO2. Upon reaching about 70% confluence, cells had their old medium substituted with fresh media, which included FITC-labeled dsMCu-D, dsMCu-D@M, and dsMCu-D@M-Co. After 2–8 h, the cells were washed three times with PBS. After fixing the cells with a 4% paraformaldehyde solution for 30 min, actin-tracker and DAPI were used to label F-actin and the nucleus, respectively. Finally, images were captured using a Nikon microscope (Nikon Eclipse Ti-S, USA). Cells undergoing various treatments were also examined using bio-TEM.

Cytotoxicity analysis in vitro

BxPC-3 cells were allocated to 96-well plates at a seeding rate of 5×10^3 cells per well and permitted 24 h to settle and adhere. Post-adhesion, these cells received treatments with variable concentrations of DSF, CuET, dsMN, dsMCu, dsMCu-D, dsMCu-D@M, and dsMCu-D@M-Co for a duration of 12 h. Subsequent to the treatment period, 20 μL of MTT reagent (5 mg/mL) was added to each well, followed by a further incubation of four hours. After this incubation, the medium was evacuated, and 50 μL of DMSO was introduced to each well to solubilize the formazan deposits, involving gentle agitation for 15 min. The absorbance of each well was then quantified at 570 nm using a Bio-Rad Model 680 Microplate reader. To assess cellular viability, cells in 12-well plates were incubated for 12 h, then stained with Calcein-AM and PI for 25 min at 37 °C, and observed under an inverted fluorescence microscope after the treatment. For apoptosis studies, BxPC-3 cells were arranged in 12-well plates and exposed to PBS, dsMCu, dsMCu-D, dsMCu-D@M, and dsMCu-D@M-Co (50 μg/mL) for 12 h. The cells were then released using non-EDTA trypsin, collected, and subjected to Annexin V-FITC/PI staining, followed by flow cytometry analysis to measure apoptotic activity.

Nanoparticle penetration in vitro

The 96-well plates were coated with 1.5% agarose solution, which had been heated to a high temperature. The setup was incubated at 37 °C for 24 h. The BxPC-3 cells were seeded into the agarose-coated wells at a concentration of 1×10^3 cell/well. After seven days of incubation, BxPC-3 MCSs were developed and those ranging in size to ~200 μm in diameter were chosen for continued testing. To test the ability of the nano platform to penetrate, the prepared BxPC-3 MCS was placed into a confocal dish with 1 mL of the new medium; this was about a new medium that had been labelled with FITC forms of dsMCu-D, dsMCu-D@M, and dsMCu-D@M-Co. The CLSM technique was employed to perform Z-stack scanning at every five μm from the top to bottom of the MCS after 24 h of incubation. The MCS was dissociated into single cells with accurate reagent, and FITC-positive cells and fluorescence intensity were measured using flow cytometry. In the study of MCS growth inhibition, the prepared BxPC-3 MCSs were co-incubated with dsMCu, dsMCu-D, dsMCu-D@M, and dsMCu-D@M-Co at a concentration of 50 μg/ml. The MCSs remained in culture for five days, during which their development was traced and recorded based on photographs taken by an optical microscope.

Assessment of nanoparticles triggered DLAT aggregation by CLSM

The BxPC-3 cells were seeded and cultured in an 8-chamber slide for 24 h. Subsequently, five treatments were administered: PBS, dsMCu, dsMCu-D, dsMCu-D@M, and dsMCu-D@M-Co. Following this, the cells were washed with cold PBS and fixed with 4%

paraformaldehyde for 30 min. Subsequently, Triton X-100 was applied for 10 min to ensure proper permeabilization. After blocking with a blocking buffer for 2 h, the primary antibody to DLAT was incubated with the cells overnight at 4 °C. Following a PBS wash, the cells were incubated with the corresponding secondary antibody for 2 h at room temperature. DAPI and actin-tracker were utilized to label the nucleus and F-actin, respectively. Finally, fluorescent images were captured using CLSM.

Western blot analysis

Cell cultures were separated, using different treatments at a temperature of 37 °C. Following a 12-hour incubation period, the cells were washed extensively using PBS at low temperature and subsequently subjected to lysis using RIPA buffer for lysis. These lysed samples were centrifuged at 12,000 rpm at 4 °C for 15 min. 20 μg of protein in each lane was isolated through 10% SDS-PAGE. The isolated proteins were moved onto a polyvinylidene fluoride (PVDF) membrane and obstructed using 5% skim milk powder for 2 h at ambient temperature. Subsequently, this membrane was subjected to overnight incubation with primary antibodies including DLAT, LIAS, NPLOC4 and β-actin. Subsequently, this membrane was additionally exposed to the HRP-labeled goat anti-rabbit secondary antibody for 2 h at a temperature of 4 °C. An image was taken using a molecular imager (ChemiDoc Touch Imaging System, Bio-Rad, USA).

Detection of mitochondrial membrane potential and ROS production

BxPC-3 cells were cultured in an 8-chamber slide at 37 °C for 24 h prior to applying various treatments. Eventually, the cells were stained with the JC-1 probe and imaged using CLSM.BxPC3 cells were seeded into 8-chamber slide and cultured at 37 °C for 24 h. Afterwards, cells were incubated with PBS, dsMCu, dsMCu-D, dsMCu-D@M, and dsMCu-D@M-Co. Cells were washed with PBS after endocytosis and incubated with DCFH-DA for 20 min at 37 °C. The intracellular oxidized DCF could be used as the indicator of ROS generation. The corresponding fluorescence images of intracellular DCF at excitation wavelength of 488 nm were taken by CLSM. Moreover, the cells could be collected and analyzed by flow cytometry in addition to FCM observation.

Blood compatibility test

2 mL whole mouse blood was taken from the BALB/c nude mice and added into the anticoagulant tube. After centrifugation (3000 rpm, 5 min) and washing the sediment with PBS five times, the red blood cells were collected and then diluted with PBS three times. 100 μL of the above diluted red blood cells were added to tubes containing 900 μL of dsMCu, dsMCu-D, dsMCu-D@M, and dsMCu-D@M-Co solution, ultrapure water, or PBS and mixed evenly. After incubation at 37 °C for 2 h, the mixtures were centrifuged at 10,000 rpm for 5 min, and the UV absorbance of each tube at 540 nm was measured.

In vivo biodistribution

BxPC-3 tumor-bearing mice ($n=3$ per group) were randomly assigned to receive intravenous injections of Cy5.5-labeled dsMCu-D, dsMCu-D@M, or dsMCu-D@M-Co (10 mg/kg). The mice underwent in vivo imaging using the IVIS Spectrum fluorescence imaging system (Caliper, USA) at 12-, 24-, and 48-hours post-injection. At the final time point, tumors and major organs (heart, liver, spleen, lung, and kidneys) were collected for ex vivo biodistribution analysis. Copper content was quantified using ICP-MS.

In vitro and in vivo MRI

dsMCu-D@M-Co nanoparticles were dispersed in deionized water at copper ion concentrations ranging from 0 to 1.6 mM and then aliquoted into 1 mL Eppendorf tubes for analysis. T1-weighted images were acquired using a 3T MRI scanner (Discovery MR 750, GE, USA). For in vivo studies, the nanoparticles were administered intravenously to mice through the tail vein. Subsequent imaging was performed using a rapid spin-echo sequence with a repetition time of 400 ms, an echo time of 21 ms, a field of view of 60×60 mm, a matrix of 320×192, and a slice thickness of 2 mm.

In vivo assessment of collagen degradation and tumor penetration

To evaluate collagen degradation within tumor tissues, Masson's trichrome staining and immunofluorescence methods were employed. BxPC-3 tumor-bearing mice were euthanized 24 h post-administration of dsMCu, dsMCu-D, dsMCu-D@M, or dsMCu-D@M-Co (10 mg/kg). Tumor samples were processed into paraffin-embedded sections, were Masson's trichrome staining highlighted collagen for microscopic analysis. Furthermore, these sections underwent incubation with primary antibodies against collagen I, followed by secondary antibodies as per the staining kit's protocol. To evaluate the in vivo penetration ability of dsMCu-D@M-Co, mice bearing BxPC-3 tumors were administered intravenous injections of FITC-labeled dsMCu-D, dsMCu-D@M, and dsMCu-D@M-Co at a dosage of 10 mg/kg. Forty-eight hours post-injection, the mice were euthanized, and their tumors were promptly excised, snap-frozen, and sectioned. The sections of these tumors were then stained with DAPI and CD31 to assess penetration dynamics, which were examined using confocal laser scanning microscopy (CLSM).

In vivo antitumor effect

When the tumor reaches the desired volume, BxPC-3 tumor-bearing mice ($n=5$ per group) were randomly assigned to receive treatments including PBS, dsMCu, dsMCu-D, dsMCu-D@M, and dsMCu-D@M-Co. Injections were administered on days 1, 3, and 5. Tumor volume and body weight were recorded every two days. On day 14 post-treatment, the tumors were excised, and the survival of mice in each group was monitored for up to 60 days.

IHC and IF staining analysis

In the case of IHC staining, after dewaxing, sections underwent antigen retrieval in citrate sodium buffer at 60 °C overnight. Following this, sections were exposed to 3% H_2O_2 and obstructed using 5% bovine serum albumin (BSA) at room temperature for 1 h. The sections were incubated overnight with the corresponding primary antibodies at 4 °C. Subsequently, they were incubated with biotin-labeled secondary antibodies at room temperature for 1 h. The DAB reagent was then applied, and images for IHC were captured using a microscope. In the case of IF staining, dewaxing and antigen retrieval procedures mirrored those used in IHC staining. Following this, the sections were subjected to permeabilization using 0.1% Triton X-100 for 20 min and obstructed using 5% BSA for 1 h at room temperature. After a PBS wash, the sections were exposed to the corresponding secondary antibodies and stained with DAPI. Images for IF were obtained using a fluorescence microscope.

Statistical analysis

GraphPad Prism software was employed for statistical analysis. The findings were expressed as mean ± standard deviation (SD). Group comparisons were evaluated using both one-way analysis of variance (ANOVA) and Student's t-test, with statistical significance set at $P<0.05$. Significance levels were denoted as $^{*}p<0.05$, $^{**}p<0.01$, $^{***}p<0.001$, and $^{****}p<0.0001$.

Results and discussion

Construction and characterization of dsMCu-D@M-Co nanoparticles

Initially, highly monodisperse hollow mesoporous organosilica nanospheres dsMNs were synthesized using the "structural difference-based selective etching" method [29]. Specially, core-shell structured mesoporous SiO_2-organosilica nanoparticles (referred to as unetched dsMN, Fig. S1) were synthesized via the co-hydrolysis and co-condensation of TEOS and BTES. CTAC served as the structure-directing agent, while TEA functioned as the alkaline catalyst. Given that the Si-C bonds in the organosilica shell were more stable and stronger than the Si-O bonds in the SiO_2 core, $NH_3{\cdot}H_2O$ was employed to selectively etch the inner SiO_2 core, resulting in disulfide-bridged dsMNs. Sulfhydryl groups were introduced into the synthesized dsMNs via the grafting of MPTMS, yielding dsMN-SHs. The surface of the dsMN-SHs was then covalently linked with ultrasmall CuS via sulfydryl linkers, leading to the formation of dsMCu NPs. TEM images displayed a highly dispersed and uniformly spherical morphology as well as a hollow mesoporous structure of both dsMN and dsMCu NPs (Fig. 1A). The average size of the dsMNs was 31.65 ± 0.41 nm, which increased to 34.21 ± 0.69 nm following Cu–S conjugation (Fig. 1C). The elemental composition of the dsMCu nanoparticles was characterized using energy-dispersive X-ray spectroscopy (EDS). Analysis confirmed the presence and distribution of Si, O, Cu, and S in the nanostructures. (Figs. 1B, S2, and S3), confirming the successful introduction of Cu into the NPs framework. Furthermore, the alteration in the zeta potential from − 18.63 mv to -22.74 mv also corroborated the successful conjugation of CuS (Fig. 1C). Inductively coupled plasma mass spectrometry (ICP-MS) revealed that the engineered Cu content reached 16.37%. The successful doping of higher levels of Cu in the nanoplatform laid the foundation for subsequent cuproptosis-related tumor killing. Furthermore, the initial mesopore size of the dsMNs was 3.66 nm, which showed only a minimal change (to approximately 3.69 nm) in the dsMCu NPs, suggesting that the mesoporous channels remained unobstructed (Fig. 1D). The BET surface area of the dsMNs was 253.4 $m^2\ g^{-1}$, whereas that of the dsMCu NPs was 129.2 $m^2\ g^{-1}$, providing substantial surface areas to accommodate drug payloads. DSF was subsequently encapsulated within the hollow interior of the dsMCu NPs via physical adsorption (dsMCu-DSF, denoted as dsMCu-D); the product showed no significant changes in morphology and particle size (Fig. S5). The drug loading rate of DSF was calculated to be 10.59%, as determined by thermogravimetric analysis (Fig. S6).

FTIR spectroscopy validated the alterations in the chemical composition (Fig. 1E). The characteristic absorption peak of Cu–S bond was observed at 680.2 cm^{-1} in the dsMCu NPs; conversely, it was not detected in the dsMNs. The peaks at 1347.9 cm^{-1} and 1350.2 cm^{-1} confirmed the presence of S-S disulfide bonds in both dsMCu and dsMN nanostructures. Given the proclivity of disulfide bonds within the framework to undergo cleavage in the reductive TME, the TEM images of dsMCu NPs showed time-dependent biodegradability in GSH and acidic solutions (Fig. 1F). ICP-MS results revealed that the cumulative release of Cu^{2+} was approximately only 40% at pH of 7.4, without GSH (Fig. 1G). At lower pH values and higher GSH concentrations, over 90% of Cu^{2+} in the dsMCu-D NPs was rapidly released within 48 h. DSF in dsMCu-D NPs exhibited similar release profiles in response to pH and GSH stimulation

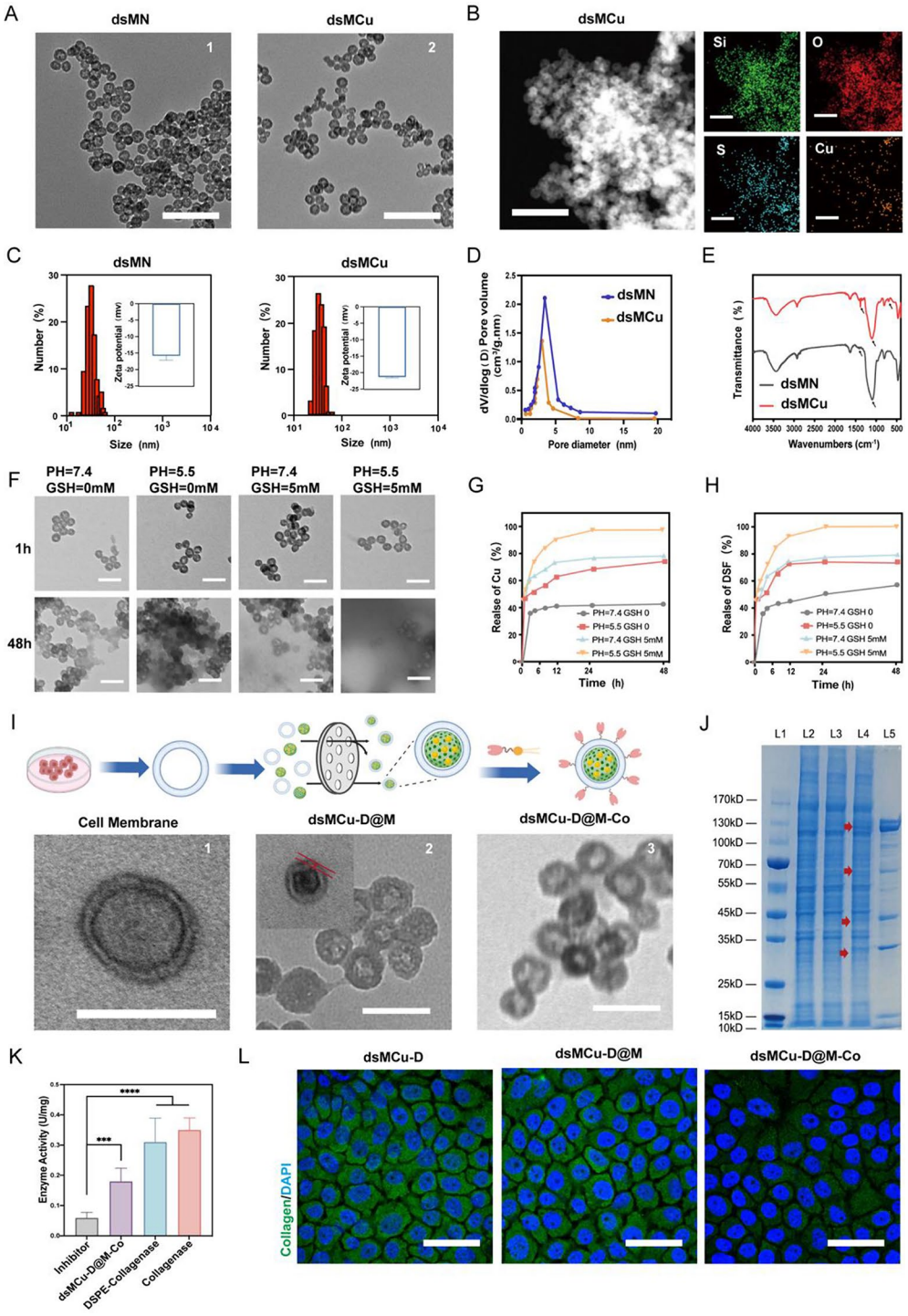

Fig. 1 Synthesis and characterization of dsMN, dsMCu, dsMCu-D, dsMCu-D@M, and dsMCu-D@M-Co. (**A**) TEM image of dsMN and dsMCu. Scale bar, 200 nm. (**B**) Elemental mapping (Si, O, S, and Cu) in dsMCu NPs. Scale bar = 200 nm. (**C**) DLS data and Zeta potential of dsMN and dsMCu. (**D**) Pore size distributions of dsMN and dsMCu. (**E**) FT-IR spectra of dsMN and dsMCu. (**F**) Representative TEM images of dsMCu after 1 h and 48 h of incubation in PBS with different pH values and GSH. Scale bar, 100 nm. (**G**-**H**) Cumulative release profiles of Cu^{2+} (**G**), and DSF (**H**) from dsMCu-D NPs in PBS with different pH values and GSH. (**I**) Scheme and TEM image of cell membrane, dsMCu-D@M, and dsMCu-D@M-Co. Scale bar, 100 nm. (**J**) SDS-PAGE protein analysis of: L1, marker; L2, cell membrane; L3, dsMCu-D@M; L4, dsMCu-D@M-Co; L5, collagenase. (**K**) Relative enzyme activities. (**L**) Collagen I expression of BxPC-3 cells treated with dsMCu-D, dsMCu-D@M, and dsMCu-D@M-Co by CLSM. Scale bar, 20 μm

(Fig. 1H). The simultaneous release of Cu^{2+} and DSF could rapidly form the toxic CuET metabolite, as evidenced by the different characteristic absorption peaks in the UV-vis spectrum. The characteristic peak of DSF was located at about 265 nm, while the characteristic peak of CuET was located at about 425 nm [36]. NIR spectra confirmed CuET formation from degraded dsMCu-D NPs, indicating effective Cu^{2+} and DSF release in situ (Fig. S7). These results indicated that the dsMCu-D NPs could respond to the TME, this TME-respond strategy allowed for controlled release of both Cu^{2+} and DSF in situ and thereby maximized the precise anti-tumor effect.

Subsequently, we employed the liposome extrusion method to uniformly coat the surface of dsMCu-D NPs (dsMCu-D@M) with the cell membranes of BxPC-3 cells [37]. Following this, the membrane surface was functionalized with DSPE-conjugated collagenase through the lipid insertion method, resulting in the formation of our final nanoplatform (dsMCu-D@M-Co). The morphologies of the resulting cell membrane, dsMCu-D@M, dsMCu-D@M-Co NPs were depicted in Fig. 1I and S8. The dsMCu-D@M NPs possessed a core–shell structure with a dsMCu-D core ensconced in a thin membrane shell (Fig. 1I 2). The thickness of the membrane shell was measured to be approximately 2.5 nm. The faint spheres surrounding the dsMCu-D@M-Co NPs confirmed the successful conjugation of collagenase (Fig. 1I 3). The degree of collagenase modification on the dsMCu-D@M-Co nanosystem was calculated using the bicinchoninic acid (BCA) assay. Unbound collagenase was separated through ultrafiltration, and its concentration was quantified using a BCA Protein Assay Kit. The modification degree of collagenase was found to be 17.42% ± 3.51%. The dsMCu-D@M-Co NPs exhibited a protein profile akin to that of the BxPC-3 cell membrane, with discernible bands of collagenase, indicating the successful translocation of membrane proteins and encapsulation of collagenase within the NPs (Fig. 1J). We then quantified the shifts in collagenase activity using a collagenase enzyme activity detection kit and a collagen gel containing FITC. The ultimate collagenase activity of dsMCu-D@M-Co NPs was estimated to be approximately 56% of the original free collagenase (Fig. 1K, S10), indicating that dsMCu-D@M-Co NPs retained a relatively high collagenase activity. Owing to the similarity between gelatin and collagen, the enzyme activity was also assessed by evaluating gelatin degradation. Pure gelatin dissolved in warm water but resolidified into a hydrogel at low temperatures [38]. Gelatin remained liquid after co-incubation with dsMCu-D@M-Co NPs, indicating that dsMCu-D@M-Co still had collagenase activity, degrading gelatin into low molecular weight products that would not solidify at low temperatures (Fig. S9). Collagen expression and degradation in the BxPC-3 cells was further investigated by confocal laser scanning microscope (CLSM). After incubation with different preparations for 12 h, the collagen content surrounding the dsMCu-D@M-Co-treated cell surface decreased significantly (Fig. 1L, S11, and S12). This proved that dsMCu-D@M-Co had the ability to significantly degrade collagen, providing evidence for our further study of ECM degradation.

Cellular uptake and penetration behavior in vitro

Bio-transmission electron microscopy (bio-TEM) and CLSM images illustrated the number of dsMCu-D@M-Co NPs in BxPC-3 cells was significantly increased compared with dsMCu-D NPs due to the homologous targeting ability of the cell membrane (Fig. 2A and B). At the same time, we also observed that long-term treatment (8 h) caused the disintegration of dsMCu-D@M-Co NPs. We believed this may be because the disulfide bonds in the dsMCu-D@M-Co responded to the high GSH environment in the PDAC cell [39]. CLSM images showed that in addition to the change in uptake over time, the fluorescence of dsMCu-D@M-Co NPs was slightly stronger than that of dsMCu-D@M NPs; this may be due to the relaxation of the dense collagen barrier by collagenase, which promoted the increase of endocytosis.

Multicellular spheroids (MCSs) were employed to assess the in vitro penetration of dsMCu-D@M-Co into PDAC tumor. MCSs more closely resembled the actual TME compared to two-dimensional (2D) models, as they facilitated the replication of cell-cell interactions and the ECM, including components such as collagen [40]. Consequently, MCSs were ideal for evaluating the permeability of dsMCu-D@M-Co NPs in vitro and could serve as a valuable reference for subsequent in vivo studies. FITC-labeled dsMCu-D@M-Co NPs were used to visualize the distribution, and the penetration behavior was observed through CLSM via z-stack imaging. Minimal fluorescence was observed in the dsMCu-D-treated MCSs (Fig. 2C), indicating limited penetration. The dsMCu-D@M-treated MCSs exhibited a slightly higher fluorescence intensity, indicating enhanced cellular uptake due to targeting of the PDAC cell membrane; however, uptake was still limited to the MCSs surface due to the hindrance of the dense ECM. The dsMCu-D@M-Co-treated MCSs exhibited notably stronger and more uniform fluorescence, nearly penetrating the entirety of the MCSs. This indicated the loosening of the ECM along the dsMCu-D@M-Co NPs diffusion path via collagen degradation, which facilitated penetration into the deep MCSs regions. The visualization of 40 μm depth sections via 2.5D diagrams clearly revealed the fluorescence intensity and distribution. Quantitative analysis demonstrated that the dsMCu-D@M-Co group exhibited the most intense fluorescence in the central MCSs. Furthermore, fluorescence activated cell sorting (FACS) analysis confirmed

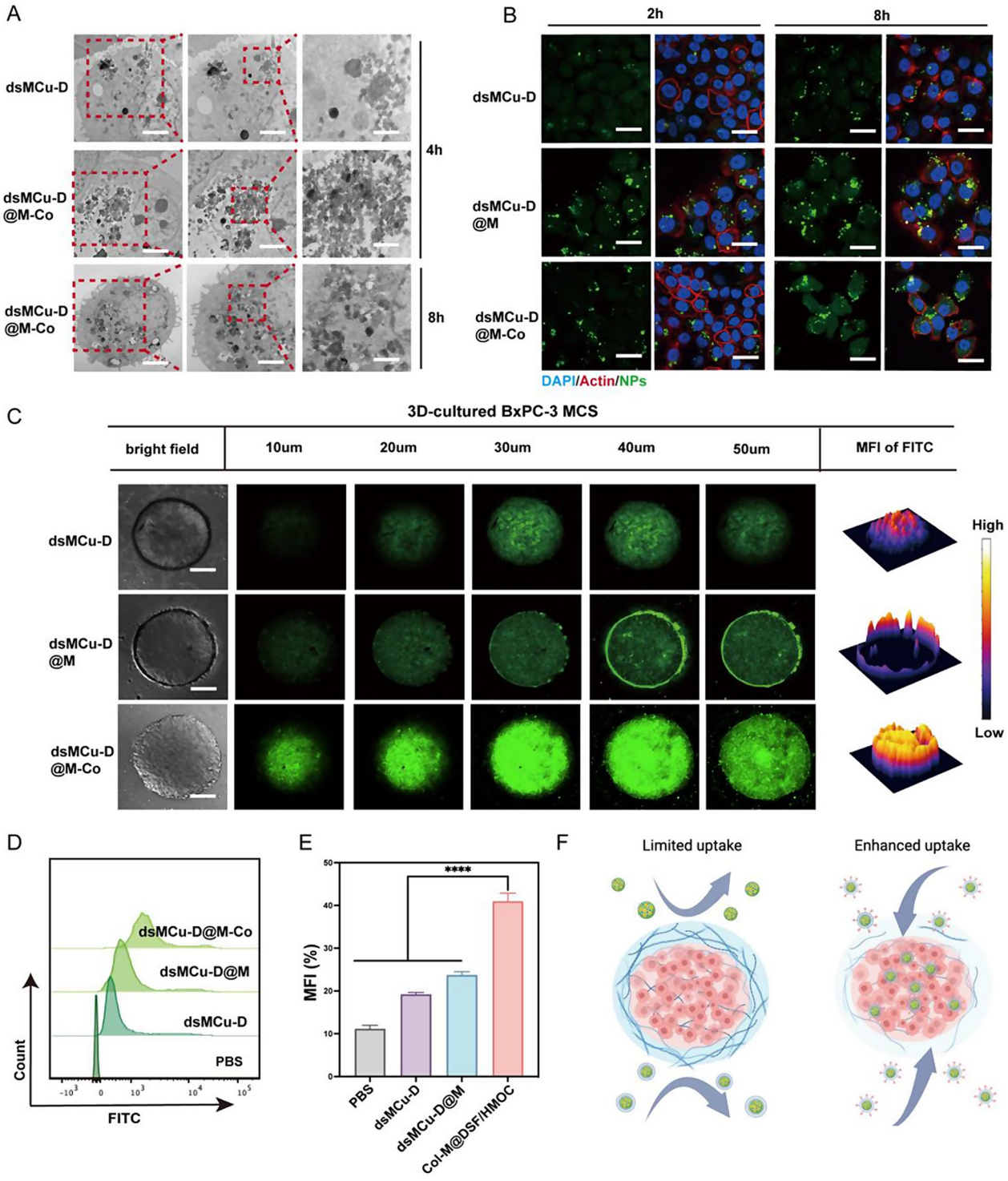

Fig. 2 Cellular uptake and digestion of collagen prompting the penetration of NPs in vitro. (**A**) TEM images of the cellular uptake of dsMCu-D and dsMCu-D@M-Co by BxPC-3 cells. Scale bar, 5 μm, 4 μm, 500 nm. (**B**) CLSM images of BxPC-3 cells treated with dsMCu-D, dsMCu-D@M, and dsMCu-D@M-Co. Scale bar, 20 μm. (**C**) CLSM z-stack images of BxPC-3 MCSs after incubation with FITC- dsMCu-D, FITC- dsMCu-D@M, and FITC- dsMCu-D@M-Co. Scale bar, 50 μm. (**D**-**E**) FACS analysis of BxPC-3 MCS cells after incubation with PBS, FITC- dsMCu-D, FITC- dsMCu-D@M, and FITC- dsMCu-D@M-Co. (**F**) Schematic of the digestion of collagen prompting the penetration of NPs in vitro

these findings, showing that the number of FITC-positive cells in the dsMCu-D@M-Co-treated group was significantly increased compared with the other groups, with even a 2.4-fold increase compared with the dsMCu-D group (Fig. 2D and E).

Cytotoxicity evaluation

To validate the Cu-dependent antitumor activity of DSF, we examined the cytotoxicity of DSF and CuET at various concentrations. MTT assays showed that in the absence of Cu, DSF exhibited extremely high cell viability even at very high concentrations. CuET, on the other hand, showed excellent PDAC cell killing effects at lower concentrations, which indicated the efficacy of DSF as a potential antitumor molecular drug in the presence of Cu (Fig. S15). Furthermore, we verified the cytotoxicity of different NPs upon PDAC cells. The cytotoxicity of dsMCu was very weak, while dsMCu-D NPs showed enhanced lethal effects, further confirming that the combination of DSF and Cu promoted the antitumor effect. More notably, the IC50 of dsMCu-D@M-Co NPs decreased significantly, and we speculated that this enhancement was attributed to cell membrane targeting and collagenase degradation, leading to more efficient drug delivery to PDAC cells. (Fig. S16).

Moreover, to exploring the impact of different preparations on MCSs growth, we examined MCSs growth after five days of treatment with various NPs (Fig. S13, S14). The dsMCu-D@M-Co group showed the most significant inhibition, leading to a marked reduction in the MCSs volume, nearly causing their disintegration and disappearance. These results exhibited that the dsMCu-D@M-Co NPs effectively permeated MCSs via collagenase-mediated ECM degradation and induced maximal cytotoxicity.

Investigation of dsMCu-D@M-Co antitumor mechanism

Cuproptosis was recorded as a type of copper-induced cell death, as we mentioned before, this stress was particularly evidenced by the aggregation of lipoylated proteins in mitochondria and the destabilization of Fe–S cluster proteins [41]. Cu directly engaged with DLAT, fostering the disulfide-bond-dependent aggregation of lipoylated DLAT. Notably, LIAS emerged as a pivotal mediator of lipoylation, contributing to the accumulation of noxious lipoylated DLAT and subsequent cell death (Fig. 3A). Moreover, the formation of CuET via the interaction of DSF with Cu^{2+} could induce apoptosis. Consequently, NPL4 protein aggregation was promoted, disrupting these specific processes and culminating in cell death. Considering the role of GSH as an inhibitor of cuproptosis, reducing GSH levels could trigger cuproptosis in PDAC cells (Fig. 3B). The disulfide bonds in dsMCu-D@M-Co had reacted with GSH, and as the dsMCu-D@M-Co fragmented, the GSH level in the TME had significantly decreased, thereby facilitating the occurrence of cuproptosis. Subsequent immunofluorescence analysis of BxPC-3 cells had revealed a significant increase in DLAT foci following treatment with dsMCu-D, dsMCu-D@M, and dsMCu-D@M-Co NPs (Fig. 3C), indicating abnormal oligomerization of DLAT. Additionally, Western blot analysis demonstrated that the expression of soluble DLAT in dsMCu-D@M-Co treated BxPC-3 cells was significantly reduced, thereby contributing to proteotoxic stress and subsequent cell death (Fig. 3D). Moreover, it was observed that LIAS was downregulated following dsMCu-D@M-Co treatment, as Cu-DSF interference with Fe-S cluster proteins led to mitochondrial toxicity and facilitated cuproptosis (Fig. 3D). In the groups treated with dsMCu-D, dsMCu-D@M, and dsMCu-D@M-Co NPs, there was a notable suppression of NPL4 protein expression compared to the control. This suppression stemmed from the antitumor activity of CuET, which was capable to induce aggregation of the NPL4 protein, consequently disrupting the metabolism of ubiquitinated proteins and precipitating cell apoptosis (Fig. 3D). It was also noted that more significant changes in protein expression were observed in the dsMCu-D@M-Co treatment group than in the dsMCu-D treatment group. This observation further revealed that the collagenase-decorated nanoplatform enhanced the therapeutic effects of cuproptosis and Cu-related apoptosis [42].

Since cuproptosis was related to mitochondrial metabolism, the mitochondrial transmembrane potential (MMP) changes in the BxPC-3 cells after treatments were confirmed through CLSM with a JC-1 fluorescence probe (Fig. 3E). The fluorescence intensity ratio of red (JC-1 aggregates indicating high MMP) to green (JC-1 monomers indicating low MMP) was computed to assess mitochondrial dysfunction. The dsMCu-treated cells exhibited minimal green fluorescence, comparable to the PBS group. This observation suggests that the antitumor effect is minimal without the modification by DSF and collagenase. In contrast, the dsMCu-D@M-Co-treated cells displayed the lowest red-to-green ratio, confirming its synergistic effect on the mitochondrial dysfunction and cell apoptosis, which was likely owing to the increased Cu accumulation. DSF is a potential anticancer agent that not only promotes cellular copper uptake but also induces ROS-dependent oxidative stress. CLSM revealed that in BxPC-3 cells, the 2′,7′-dichlorodihydrofluorescein diacetate (DCFH-DA) probe showed strong green fluorescence after NPs treatment, indicating that high levels of ROS were generated in the cells. The level of ROS in cells treated with dsMCu-D@M-Co NPs was the highest, which corroborated the results of the above MMP. We further explored this trend through

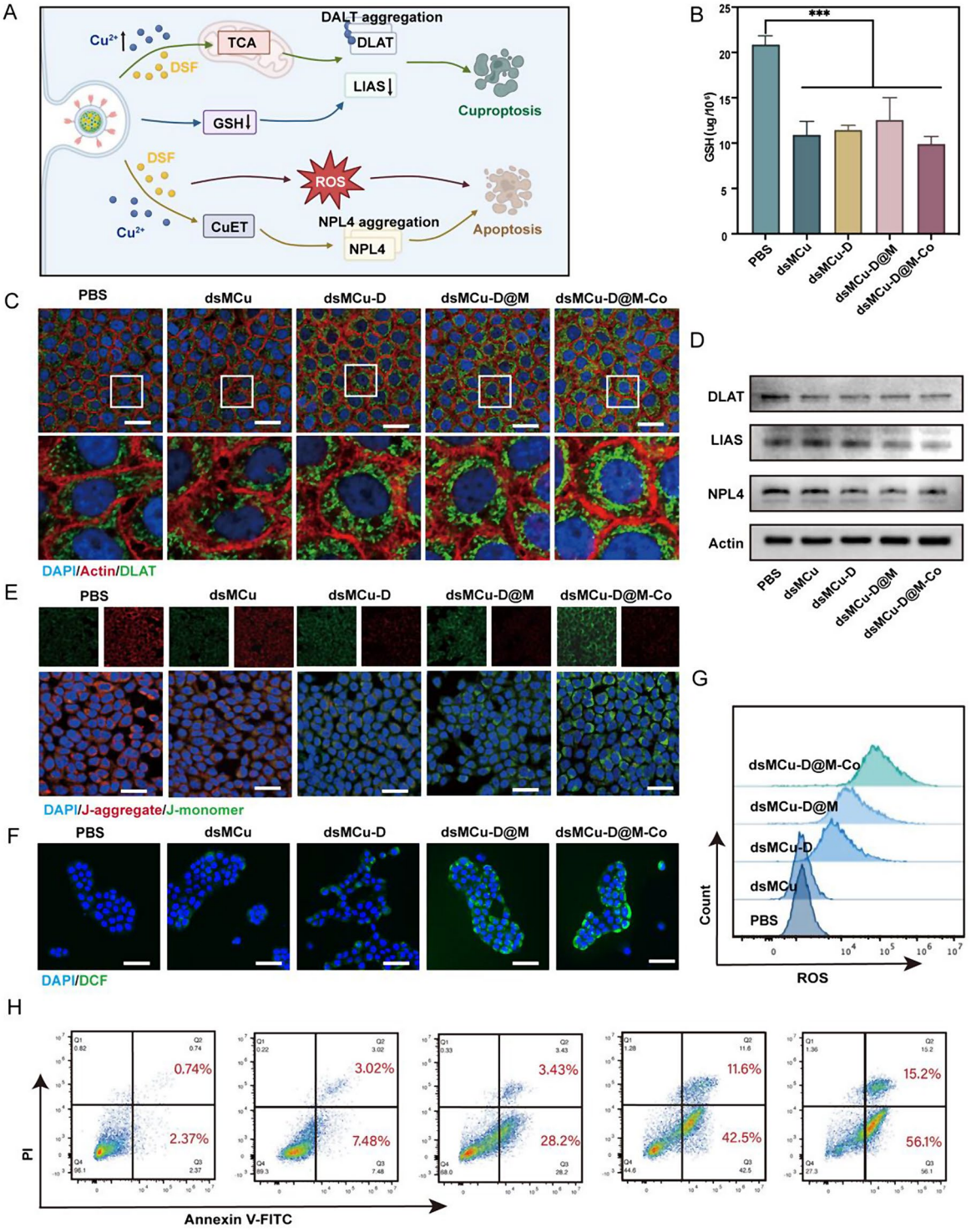

Fig. 3 Analysis of the antitumor mechanism. (**A**) Scheme for the antitumor mechanism. (**B**) GSH levels in BxPC-3 cells incubated with different treatments for 12 h. (**C**) CLSM of DLAT in BxPC-3 cells after different treatments. Scale bar = 50 μm. (**D**) Western blot analysis on the expression of DLAT, LIAS and NPL4. (**E**) CLSM of changes in mitochondrial membrane potential of BxPC-3 cells incubated with different treatments. Scale bar = 50 μm. (**F**-**G**) CLSM and FACS of intracellular ROS levels in BxPC-3 cells incubated with different treatments. Scale bar = 50 μm. (**H**) FACS analysis of the apoptosis levels of BxPC-3 cells after incubation with different treatments

FACS, which strongly demonstrated the anti-tumor efficiency of the nanoplatform at the cellular level (Fig. 3F and G). Subsequently, cytotoxicity was visually assessed through live/dead assays (Fig. S17). Most cells died in the dsMCu-D@M and dsMCu-D@M-Co groups, indicating that dsMCu-D@M and dsMCu-D@M-Co NPs effectively killed the cells via combined cuproptosis and apoptosis. The effects of apoptosis induced by various preparations were further examined by analyzing apoptotic responses (Fig. 3H, S18); the dsMCu-D@M and dsMCu-D@M-Co groups showed significant apoptosis.

dsMCu-D@M-Co biodistribution pattern in vivo

The promising in vitro antitumor effects motivated the in-depth exploration of the PDAC model. Prior to the in vivo studies, blood biochemistry assays confirmed minimal hemolysis at high concentrations, proving low risk for intravenous use (Fig. S19). Leveraging the potent tumor-cell-killing efficacy of dsMCu-D@M-Co NPs in vitro, we conducted comprehensive investigation in the BxPC3-tumor-bearing mice. Initially, we used Cy5.5-labeled NPs to assess in vivo distribution (Fig. 4A). After received intravenous injection, the BxPC3 tumor-bearing mice were allowed for real-time tracking of the formulations' biodistribution. The dsMCu-D group was widely distributed throughout the body and only showed weak fluorescence at the tumor site after 48 h. While the dsMCu-D@M and dsMCu-D@M-Co groups evidenced a significant, time-varying increase in fluorescence intensity within the tumor area starting from 12 h (Fig. 4A). This observation verified that dsMCu-D@M-Co NPs had a targeted delivery capability, allowing them to accumulate preferentially at tumor regions. Furthermore, the dsMCu-D@M-Co group exhibited significantly higher tumor fluorescence intensity than dsMCu-D@M group, signifying continuous permeation and efficient accumulation within the tumor tissue via collagenase degradation. Analysis of isolated tumors and major organs showed that the fluorescence intensity of dsMCu-D@M-Co was substantially higher in tumor tissues compared with other organs, emphasizing its tumor-specific distribution (Fig. 4B). At the same time, we also quantitatively analyzed the Cu content through ICP-MS and found that the Cu content in the tumors of the dsMCu-D@M-Co group was significantly increased (Fig. S20). These data collectively further confirmed that collagenase-decorated NPs had targeting and penetration promotion function, significantly improved the accumulation of Cu in tumor sites and amplified the anti-tumor efficiency of cuproptosis.

Tumor penetration effect and collagen degradation in vivo

Masson and collagen immunofluorescence staining showed a significantly lower collagen content of the dsMCu-D@M-Co group, indicating its potential to remodel the PDAC ECM (Fig. 4C, S23). dsMCu-D@M-Co NPs were additionally analyzed to examine whether collagen digestion at PDAC tumor might increase permeability and accumulation. We used immunofluorescence staining to visualize blood vessels, and observed colocalization of blood vessels (red) and nanomaterial formulations (green) by CLSM (Fig. 4D). In the dsMCu-D and dsMCu-D@M groups, nanomaterial fluorescence was observed only near the vessels, whereas dsMCu-D@M-Co verified notable fluorescence distant from the vessels, penetrating approximately 4.62 times deeper than the other groups (Fig. S23). To enhance the visualization of the NPs distribution, a 2.5D diagram reconstructed using ImageJ was employed for visual examination (Fig. S22). The remarkable imaging results stem from the effective collagen breakdown by dsMCu-D@M-Co NPs, prompting their relocation from the perivascular areas. The collagen degradation notably enhanced diffusion into tumors and promises an improved in vivo nanoplatform effectiveness. In summary, the degradation of collagen significantly enhanced diffusion within tumors, demonstrating considerable potential for improving the in vivo efficacy of our nanoplatform.

Investigation of T1-weight MRI in PDAC

Given the theranostic challenges in PDAC and the potential of Cu in MRI, we further explored the T1-weighted MRI performance of dsMCu-D@M-Co NPs [43, 44]. The dsMCu-D@M-Co exhibited enhanced MRI signal intensity with increasing Cu concentration in both grayscale and pseudo-color T1-weighted MRI images (Fig. S21). Post injection, dsMCu-D@M and dsMCu-D@M-Co displayed a significantly higher tumor MR signal than that of dsMCu-D, reaching a peak at 48 h (Fig. 4F). And the dsMCu-D@M-Co group showed a higher signal than that of dsMCu-D@M. This enhancement was attributed to ECM degradation and tumor targeting, which amplified the MR properties. Therefore, dsMCu-D@M-Co can gradually accumulate at the tumor site, achieving tumor targeting and strengthened T1-weighted MR imaging in vivo.

In vivo antitumor effect and biosafety

Subsequently, the therapeutic effectiveness of various formulations was evaluated in mice bearing BxPC-3 tumors. (Figure 5A and B and S26). Cu-based nanosystems dsMCu and dsMCu-D, as TME responsive monotherapies of cuproptosis, demonstrated only moderate effects on tumor recession compared to the PBS control. This outcome highlighted the limitations of non-specific targeting and dense ECM in pancreatic tumors. Owing to its ECM degradation ability and the targeting effect, the dsMCu-D@M-Co group exhibited the most substantial

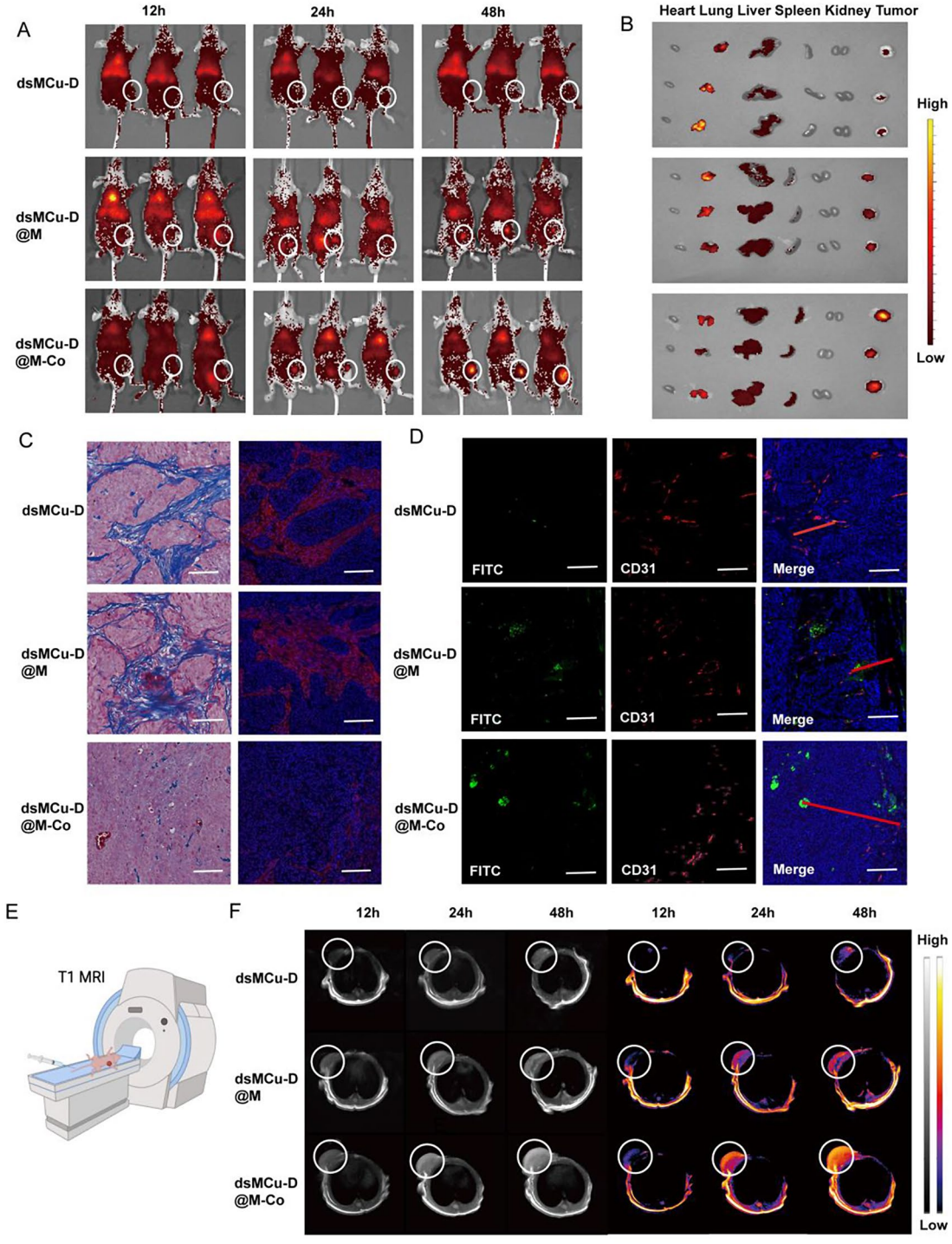

Fig. 4 Evaluation of in vivo tumor penetration, targeting capacity, and T1 MRI capability. (**A**) In vivo fluorescence images of BxPC-3 tumor-bearing mice at different time points after intravenous injection of Cy5-dsMCu-D, Cy5-dsMCu-D@M, and Cy5-dsMCu-D@M-Co. (**B**) Ex vivo fluorescence biodistribution in main organs and tumors after intravenous injection of Cy5-dsMCu-D, Cy5-dsMCu-D@M, and Cy5-dsMCu-D@M-Co. (**C**) Masson's trichrome analysis (collagen are blue) and immunofluorescence images of collagen I (red) in tumor slices. Scale bar, 100 μm. (**D**) CLSM images of tumor slices collected from mice receiving dsMCu-D, dsMCu-D@M, and dsMCu-D@M-Co. Scale bar, 100 μm. (**E**-**F**) In vivo T1-weighted MRI of BxPC3 tumor-bearing mice at different time points after intravenous injection of dsMCu-D, dsMCu-D@M, and dsMCu-D@M-Co

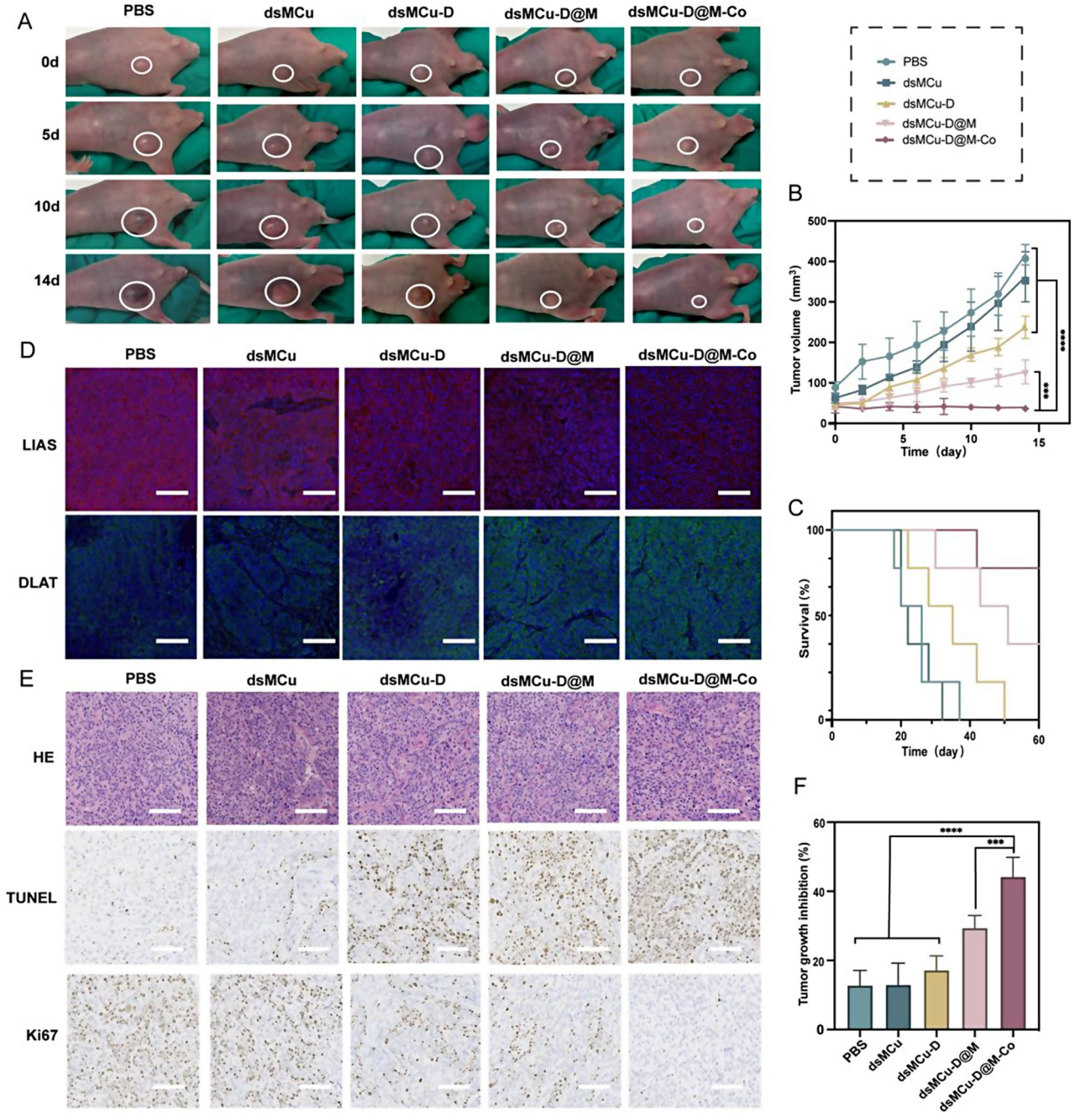

Fig. 5 In-vivo antitumor efficiency and mechanism of the BxPC-3 pancreatic tumor-bearing BALB/c mice model. (**A**) Digital photographs of the BxPC-3 pancreatic tumor-bearing mice and their tumor regions after different treatments. (**B**) Tumor growth curves during different treatments ($n=5$). (**C**) Survival rate of BxPC3 tumor-bearing mice after receiving different treatments in 60 days ($n=5$). (**D**) LIAS and DLAT staining of tumors after the mice received different treatments. Scale bar, 100 μm (**E**) H&E, TUNEL, and Ki67 staining of tumors after the mice received different treatments. Scale bar, 100 μm (**F**) Tumor growth inhibition after receiving the different treatments ($n=5$)

inhibition of tumor growth, suggesting a superior antitumor effect. Histological analysis using hematoxylin and eosin (H&E) staining demonstrated increased necrotic damage and nuclear condensation in tumor tissues treated with dsMCu-D@M-Co compared to those subjected to other groups. Additionally, evaluations of apoptosis and proliferation using terminal deoxynucleotidyl transferase dUTP nick end labeling (TUNEL) and Ki-67 immunohistochemistry demonstrated that dsMCu-D@M-Co achieved its antitumor effects by enhancing apoptosis and suppressing malignant cell proliferation (Fig. 5C). To gain deeper insights into the antitumor and antimetastatic mechanisms of dsMCu-D@M-Co, immunofluorescence assays were conducted to examine the

expression of related proteins (DLAT and LIAS) in tumor tissues [45]. Consistent with our in vitro results, the most significant accumulation of DLAT and reduction of LIAS were observed in tumor sections treated with dsMCu-D@M-Co, thereby substantiating the occurrence of cuproptosis (Fig. 5D). Survival analysis revealed that the dsMCu-D@M-Co treatment significantly prolonged survival in relation to the other modalities. These findings demonstrated that dsMCu-D@M-Co NPs directly targeted the tumor site, infiltrated the tumor tissue, and exerted potent antitumor effects in vivo. Given that the dsMCu-D@M-Co nanomedicine was engineered for the co-delivery of collagenase and Cu-DSF, its biological safety was crucial for in vivo applications [46]. Evaluations of this nanomedicine's safety profile yielded promising results. After the treatment period, histological examination of major organs from the treated mice, conducted using H&E staining, displayed no notable histological abnormalities (Fig. S24). Additionally, blood biochemistry assays indicated that the delivery systems did not cause significant changes in blood indices or impair hepatorenal functions (Fig. S27). The biological safety of dsMCu-D@M-Co can be attributed to the biocompatible dsMNs core and the membrane-mediated tumor-targeting capability, emphasizing its potential for dual Cu-specific tumor theragnostic.

Conclusion

In summary, we successfully developed a collagenase-decorated Cu-based core-shell nanoplatform, serving as an effective theranostic treatment for highly malignant PDAC. Due to the disulfide bonds within the dsMCu-D core and the PDAC cell membrane shell between dsMCu-D and collagenase, dsMCu-D@M-Co demonstrated excellent GSH responsiveness and tumor targeting. Additionally, the substantial Cu and DSF loaded on dsMCu-D@M-Co could be efficiently delivered into PDAC cells to form cytotoxic CuET. The biological activity of the collagenase on the dsMCu-D@M-Co NPs was also effectively preserved. In vitro analysis revealed that dsMCu-D@M-Co could digest collagen in tumor tissues, effectively broke through the physical barrier of PDAC, significantly enhancing NPs penetration. Furthermore, the dsMCu-D@M-Co NPs not only promoted cuproptosis initiated by disturbing the intracellular Cu balance but also apoptosis through ROS-mediated oxidative stress, effectively enhancing their anti-tumor capabilities. In vivo assays further validated that treatment with dsMCu-D@M-Co led to favorable therapeutic results in curbing tumor growth and acted as an outstanding T1-weighted MRI agent, emphasizing its viability as a safe and robust theranostic nanoagent. Overall, our results proved effective in developing multifunctional nanotheranostics of PDAC, potentially applicable to a wider range of solid tumor treatments.

Supplementary Information

The online version contains supplementary material available at https://doi.org/10.1186/s12951-024-02968-6.

Supplementary Material 1

Acknowledgements

We would like to thank the members of Professor Tang's team (Department of Chemistry, Zhejiang University) for their guidance and assistance in this study.

Author contributions

Y N W and Q M Z conceived the study and drafted the manuscript. R S Y, H Z B and G P T helped critically revise the manuscript for important intellectual content. W P L, X Y Y, J G Z and Y J L performed the research. J M, J Y C, F W and J H helped analyze data. All authors reviewed the manuscript.

Funding

This study was supported in part by grants from the National Natural Science Foundation of China (General Program: 82171998, 22175153 and 52073248), the Fundamental Research Funds for the Central Universities (226-2022-00221), and the Natural Science Foundation of Zhejiang province (LZ22H180002).

Data availability

No datasets were generated or analysed during the current study.

Declarations

Ethical approval

All the animal experiments were in line with the ARRIVE guidelines and were carried out according to the National Institutes of Health (NIH, USA) protocols, approved by the guidelines of the Ethical Committee of Zhejiang University.

Patient consent

Not applicable.

Permission to reproduce material from other sources

Not applicable.

Clinical trial registration

Not applicable.

Competing interests

The authors declare no competing interests.

Author details

[1]Department of Radiology, Second Affiliated Hospital, School of Medicine, Zhejiang University, 88 Jiefang Road, Hangzhou, Zhejiang 310009, People's Republic of China
[2]Department of Chemistry, Zhejiang University, Hangzhou 310028, People's Republic of China
[3]The First School of Clinical Medicine, Zhejiang Chinese Medical University, Hangzhou, People's Republic of China
[4]Department of Neurosurgery, First Affiliated Hospital, School of Medicine, Zhejiang University, 79 Qingchun Road, Hangzhou, Zhejiang 310009, People's Republic of China

Received: 17 August 2024 / Accepted: 3 November 2024
Published online: 10 November 2024

References

1. Halbrook CJ, Lyssiotis CA, Di Pasca M, Maitra A. Pancreatic Cancer: advances and challenges. Cell. 2023;186(8):1729–54.

2. Del Chiaro M, Sugawara T, Karam SD, Messersmith W. A. Advances in the Management of Pancreatic Cancer. *BMJ* 2023, e073995.
3. Bu L-L, Yan J, Wang Z, Ruan H, Chen Q, Gunadhi V, Bell RB. Gu, Z. advances in Drug Delivery for Post-surgical Cancer Treatment. Biomaterials. 2019;219:119182.
4. Christenson ES, Jaffee E, Azad NS. Current and emerging therapies for patients with Advanced Pancreatic Ductal Adenocarcinoma: a Bright Future. Lancet Oncol. 2020;21(3):e135–45.
5. Connor AA, Gallinger S. Pancreatic Cancer evolution and heterogeneity: integrating Omics and Clinical Data. Nat Rev Cancer. 2022;22(3):131–42.
6. Masamune A, Kikuta K, Watanabe T, Satoh K, Hirota M, Hamada S, Shimosegawa T. Fibrinogen induces cytokine and Collagen Production in pancreatic stellate cells. Gut. 2009;58(4):550–9.
7. Xie Y, Hang Y, Wang Y, Sleightholm R, Prajapati DR, Bader J, Yu A, Tang W, Jaramillo L, Li J, Singh RK, Oupický D. Stromal modulation and treatment of metastatic pancreatic Cancer with local Intraperitoneal Triple miRNA/siRNA Nanotherapy. ACS Nano. 2020;14(1):255–71.
8. Bulle A, Lim K-H. Beyond just a tight fortress: contribution of stroma to epithelial-mesenchymal transition in pancreatic Cancer. Signal Transduct Target Ther. 2020;5(1):249.
9. Mucciolo G, Araos Henríquez J, Jihad M, Pinto Teles S, Manansala JS, Li W, Ashworth S, Lloyd EG, Cheng PSW, Luo W, Anand A, Sawle A, Piskorz A, Biffi G. EGFR-Activated myofibroblasts promote metastasis of pancreatic Cancer. Cancer Cell. 2024;42(1):101–e11811.
10. Hosein AN, Brekken RA, Maitra A. Pancreatic Cancer stroma: an update on therapeutic targeting strategies. Nat Rev Gastroenterol Hepatol. 2020;17(8):487–505.
11. Yong T, Wei Z, Gan L, Yang X. Extracellular-vesicle-based drug Delivery systems for enhanced Antitumor therapies through modulating the Cancer-Immunity cycle. Adv Mater. 2022;34(52):2201054.
12. Cao J, Wu J, Yang P, Qian K, Cheng Y, Xu M, Sheng D, Meng R, Wang T, Li Y, Wei Y, Zhang Q. Dual enzyme Cascade-activated Popcorn-Like nanoparticles efficiently remodeled stellate cells to alleviate pancreatic desmoplasia. ACS Nano. 2023;17(20):19793–809.
13. Han X, Li Y, Xu Y, Zhao X, Zhang Y, Yang X, Wang Y, Zhao R, Anderson GJ, Zhao Y, Nie G. Reversal of pancreatic desmoplasia by re-educating stellate cells with a Tumour Microenvironment-activated Nanosystem. Nat Commun. 2018;9(1):3390.
14. Tian C, Huang Y, Clauser KR, Rickelt S, Lau AN, Carr SA, Vander Heiden MG, Hynes RO. Suppression of pancreatic ductal adenocarcinoma growth and metastasis by Fibrillar Collagens Produced selectively by Tumor cells. Nat Commun. 2021;12(1):2328.
15. Fan D, Cao Y, Cao M, Wang Y, Cao Y, Gong T. Nanomedicine in Cancer Therapy. Signal Transduct Target Ther. 2023;8(1):293.
16. Xu F, Huang X, Wang Y, Zhou SA, Size-Changeable. Collagenase-modified Nanoscavenger for increasing Penetration and Retention of Nanomedicine in Deep Tumor tissue. Adv Mater. 2020;32(16):1906745.
17. Zinger A, Koren L, Adir O, Poley M, Alyan M, Yaari Z, Noor N, Krinsky N, Simon A, Gibori H, Krayem M, Mumblat Y, Kasten S, Ofir S, Fridman E, Milman N, Lübtow MM, Liba L, Shklover J, Shainsky-Roitman J, Binenbaum Y, Hershkovitz D, Gil Z, Dvir T, Luxenhofer R, Satchi-Fainaro R, Schroeder A. Collagenase nanoparticles enhance the penetration of drugs into pancreatic tumors. ACS Nano. 2019;13(10):11008–21.
18. Ge EJ, Bush AI, Casini A, Cobine PA, Cross JR, DeNicola GM, Dou QP, Franz KJ, Gohil VM, Gupta S, Kaler SG, Lutsenko S, Mittal V, Petris MJ, Polishchuk R, Ralle M, Schilsky ML, Tonks NK, Vahdat LT, Van Aelst L, Xi D, Yuan P, Brady DC, Chang CJ. Connecting copper and Cancer: from transition metal signalling to Metalloplasia. Nat Rev Cancer. 2022;22(2):102–13.
19. Yang S, Song Y, Hu Y, Chen H, Yang D, Song X. Multifaceted roles of copper ions in Anticancer Nanomedicine. Adv Healthc Mater. 2023;12(23):2300410.
20. Tsvetkov P, Coy S, Petrova B, Dreishpoon M, Verma A, Abdusamad M, Rossen J, Joesch-Cohen L, Humeidi R, Spangler RD, Eaton JK, Frenkel E, Kocak M, Corsello SM, Lutsenko S, Kanarek N, Santagata S, Golub TR. Copper induces cell death by targeting lipoylated TCA cycle proteins. Science. 2022;375(6586):1254–61.
21. Kahlson MA, Dixon SJ. Copper-Induced Cell Death. Science. 2022;375(6586):1231–2.
22. Lener MR, Scott RJ, Wiechowska-Kozłowska A, Serrano-Fernández P, Baszuk P, Jaworska-Bieniek K, Sukiennicki G, Marciniak W, Muszyńska M, Kładny J, Gromowski T, Kaczmarek K, Jakubowska A, Lubiński J. Serum concentrations of selenium and copper in patients diagnosed with pancreatic Cancer. Cancer Res Treat. 2016;48(3):1056–64.
23. Xie J, Yang Y, Gao Y, He J. Cuproptosis: mechanisms and links with cancers. Mol Cancer. 2023;22(1):46.
24. Ni C, Ouyang Z, Li G, Liu J, Cao X, Zheng L, Shi X, Guo RA. Tumor Microenvironment-Responsive Core-Shell Tecto Dendrimer Nanoplatform for magnetic resonance imaging-guided and cuproptosis-promoted chemo-chemodynamic therapy. Acta Biomater. 2023;164:474–86.
25. McMahon A, Chen W, Li F. Old wine in new bottles: Advanced Drug Delivery systems for Disulfiram-Based Cancer Therapy. J Controlled Release. 2020;319:352–9.
26. Kang X, Jadhav S, Annaji M, Huang C-H, Amin R, Shen J, Ashby CR, Tiwari AK, Babu RJ, Chen P. Advancing Cancer Therapy with Copper/Disulfiram nanomedicines and Drug Delivery systems. Pharmaceutics. 2023;15(6):1567.
27. Skrott Z, Mistrik M, Andersen KK, Friis S, Majera D, Gursky J, Ozdian T, Bartkova J, Turi Z, Moudry P, Kraus M, Michalova M, Vaclavkova J, Dzubak P, Vrobel I, Pouckova P, Sedlacek J, Miklovicova A, Kutt A, Li J, Mattova J, Driessen C, Dou QP, Olsen J, Hajduch M, Cvek B, Deshaies RJ, Bartek J. Alcohol-abuse drug disulfiram targets Cancer via P97 segregase adaptor NPL4. Nature. 2017;552(7684):194–9.
28. Abaei S, Tarighatnia A, Mesbahi A, Aghanejad A. Antibody conjugates as CT/MRI theranostics for diagnosis of cancers: a review of recent trends and advances. Sens Diagn. 2024;3(9):1428–41.
29. Tarighatnia A, Foroughi-Nia B, Nader ND, Aghanejad A. Recent trends and advances in nanosystems with tyrosine kinase inhibitors for image-guided Cancer treatments. J Drug Deliv Sci Technol. 2023;88:104938.
30. Bennett KM, Jo J, Cabral H, Bakalova R, Aoki I. MR Imaging techniques for Nano-Pathophysiology and Theranostics. Adv Drug Deliv Rev. 2014;74:75–94.
31. Li L, Yang Z, Fan W, He L, Cui C, Zou J, Tang W, Jacobson O, Wang Z, Niu G, Hu S, Chen X. In situ Polymerized Hollow Mesoporous Organosilica Biocatalysis Nanoreactor for enhancing ROS-Mediated anticancer therapy. Adv Funct Mater. 2020;30(4):1907716.
32. Zhang H, Song F, Dong C, Yu L, Chang C, Chen Y. Co-delivery of Nanoparticle and Molecular Drug by Hollow Mesoporous Organosilica for Tumor-activated and photothermal-augmented chemotherapy of breast Cancer. J Nanobiotechnol. 2021;19(1):290.
33. Jia X, Wang L, Feng X, Liu W, Wang X, Li F, Liu X, Yu J, Yu B, Yu X. Cell membrane-coated oncolytic adenovirus for targeted treatment of Glioblastoma. Nano Lett. 2023;23(23):11120–8.
34. Luo J, Cao J, Ma G, Wang X, Sun Y, Zhang C, Shi Z, Zeng Y, Zhang T, Huang P. Collagenase-loaded H-TiO_2 nanoparticles enhance Ultrasound Imaging-guided Sonodynamic Therapy in a pancreatic carcinoma xenograft model via digesting stromal barriers. ACS Appl Mater Interfaces. 2022;14(36):40535–45.
35. Lu N, Fan W, Yi X, Wang S, Wang Z, Tian R, Jacobson O, Liu Y, Yung BC, Zhang G, Teng Z, Yang K, Zhang M, Niu G, Lu G, Chen X. Biodegradable Hollow Mesoporous Organosilica Nanotheranostics for mild Hyperthermia-Induced bubble-enhanced oxygen-sensitized Radiotherapy. ACS Nano. 2018;12(2):1580–91.
36. Huo T, Zhang X, Qian M, Nie H, Liang D, Lin C, Yang Y, Guo W, Lächelt U, Huang RA. Space-Time Conversion vehicle for programmed Multi-drugs delivery into pancreatic tumor to overcome Matrix and Reflux barriers. Adv Sci. 2022;9(20):2200608.
37. Chai Z, Ran D, Lu L, Zhan C, Ruan H, Hu X, Xie C, Jiang K, Li J, Zhou J, Wang J, Zhang Y, Fang RH, Zhang L, Lu W. Ligand-modified cell membrane enables the targeted delivery of drug nanocrystals to Glioma. ACS Nano. 2019;13(5):5591–601.
38. Yang J, Ma S, Xu R, Wei Y, Zhang J, Zuo T, Wang Z, Deng H, Yang N, Shen Q. Smart Biomimetic Metal Organic frameworks based on ROS-Ferroptosis-glycolysis regulation for enhanced Tumor Chemo-Immunotherapy. J Control Release off J Control Release Soc. 2021;334:21–33.
39. Wang T, Chen G, Zhang S, Li D, Wei G, Zhao X, Liu Y, Ding D, Zhang X. Steerable microneedles enabling deep delivery of Photosensitizers and CRISPR/Cas9 systems for Effective Combination Cancer Therapy. Nano Lett. 2023;23(17):7990–9.
40. Wang L, Dou J, Jiang W, Wang Q, Liu Y, Liu H, Wang Y. Enhanced intracellular transcytosis of nanoparticles by Degrading Extracellular Matrix for Deep tissue Radiotherapy of pancreatic adenocarcinoma. Nano Lett. 2022;22(17):6877–87.
41. Lewis DJ, Deshmukh P, Tedstone AA, Tuna F, O'Brien P. On the Interaction of copper (II) with Disulfiram. Chem Commun. 2014;50(87):13334–7.
42. Jia W, Tian H, Jiang J, Zhou L, Li L, Luo M, Ding N, Nice EC, Huang C, Zhang H. Brain-targeted HFn-Cu-REGO Nanoplatform for Site-Specific Delivery and Manipulation of Autophagy and Cuproptosis in Glioblastoma. Small. 2023;19(2):2205354.

43. Mohaghegh S, Tarighatnia A, Omidi Y, Barar J, Aghanejad A, Adibkia K. Multifunctional magnetic nanoparticles for MRI-Guided co-delivery of Erlotinib and L-Asparaginase to Ovarian Cancer. J Microencapsul. 2022;39(4):394–408.
44. Holbrook RJ, Rammohan N, Rotz MW, MacRenaris KW, Preslar AT, Meade TJ. Gd (III)-Dithiolane gold nanoparticles for T_1 -Weighted magnetic resonance imaging of the pancreas. Nano Lett. 2016;16(5):3202–9.
45. Huang L, Zhu J, Xiong W, Feng J, Yang J, Lu X, Lu Y, Zhang Q, Yi P, Feng Y, Guo S, Qiu X, Xu Y, Shen Z. Tumor-generated reactive oxygen species storm for high-performance ferroptosis therapy. ACS Nano. 2023;17(12):11492–506.
46. Zhou J, Yu Q, Song J, Li S, Li X, Kang BK, Chen H, Xu J. Photothermally triggered copper payload release for cuproptosis-promoted Cancer synergistic therapy. Angew Chem Int Ed. 2023.

Publisher's note